https://doi.org/10.5194/egusphere-2026-4501
Preprint. Discussion started: 17 August 2026

Synergistic retrieval of atmospheric boundary layer height from multi-source observations over the Arctic Ocean during MOSAiC

Yuliang Liu[1,2] , Shulei Li*[1,2], Lei Liu[1,2],Shuai Hu[1,2], Xuyang Li[1,2], Rongying Shao[1,2]

[1] *College of Meteorology and Oceanography, National University of Defense Technology, Changsha, China*
[2] *Key Laboratory of High Impact Weather(special), China Meteorological Administration, Changsha, China*

Correspondence to: Shulei Li (lishulei@nudt.edu.cn)

Abstract. Continuous observations of the central Arctic boundary layer (ABL) remain scarce, and ABL structure is strongly governed by stability, clouds, and wind shear. Using the year-round MOSAiC record, a condition-adaptive, multi-source neural network is developed to retrieve atmospheric boundary layer height (ABLH) from microwave radiometer, infrared hyperspectral radiances, ceilometer backscatter, wind profiles. Overall RMSE of 42.4 m is achieved, with best performance under clear skies and weakest under cloudy conditions. Feature-attribution and ablation analyses indicate wind-field information provides the strongest ABLH constraint. Clear-sky retrievals are improved by infrared observations, but cloud-related interference is introduced under cloudy conditions, whereas cloudy-scene robustness is enhanced by microwave observations. The ABLH annual cycle is found to peak in May and reach minima in August and December, mainly controlled by boundary-layer thermal evolution, cloud frequency, and low-level jets. Daily mean ABLH is closely linked to surface temperature, especially in spring and autumn. Stable and neutral boundary layers dominate: stable cases occur more often when cloud base lies above the ABL, while neutral cases are more frequent when cloud base lies below it. ABL development is promoted by wind shear beneath low-level jets, which increases with jet-core wind speed; wind shear stress, friction velocity, and downward longwave radiation also contribute. Model generalizability is confirmed by extrapolation to other Arctic sites and representative case studies. Overall, complementary active and passive remote-sensing observations are effectively integrated to generate continuous, condition-aware ABLH retrievals in complex Arctic environments, supporting characterization of boundary-layer variability and Arctic atmosphere–surface interactions.

1 INTRODUCTION

The atmospheric boundary layer (ABL) is the turbulent layer of the atmosphere that is directly influenced by the Earth surface, and its structure regulates the exchange of energy, moisture, momentum, and tracers between the surface and the free atmosphere (Stull, 1988; Marsik et al., 1995). In the Arctic, the boundary layer is particularly important because it mediates the coupling among the ocean, sea ice, snow-covered surfaces, clouds, and the overlying atmosphere (Jozef et al., 2023). Through the exchange of momentum, heat, moisture, and aerosols, Arctic boundary-layer processes directly affect the

https://doi.org/10.5194/egusphere-2026-4501
Preprint. Discussion started: 17 August 2026

surface energy budget, cloud formation and persistence, sea-ice evolution, and the regional climate system (Heinemann et al., 2023; Jozef et al., 2022). A process-level and quantitative understanding of boundary-layer dynamics is therefore essential not only for Arctic climate research, but also for a wide range of applications with substantial societal, economic, and health implications, including air-quality assessment (e.g., Han et al., 2009; Stirnberg et al., 2021; Sujatha et al., 2016), greenhouse gas monitoring (e.g., Lauvaux et al., 2016), numerical weather prediction (e.g., Illingworth et al., 2019), and transportation safety, including Arctic shipping (e.g., Vajda et al., 2011). The importance of the Arctic boundary layer has become increasingly evident in the context of rapid Arctic climate change and substantial sea-ice loss over recent decades (Matveeva and Semenov, 2022). Arctic sea surface temperature is increasing at approximately two to three times the global mean rate (Rantanen et al., 2023), and this amplified warming is closely linked to atmospheric boundary-layer processes over the Arctic Ocean (Graversen et al., 2008; Akansu et al., 2023). However, the thermodynamic and dynamic structures of the Arctic boundary layer remain insufficiently characterized, which contributes to substantial uncertainties and biases in numerical weather prediction at high latitudes (Xi et al., 2024; Jozef et al., 2014; Wesslén et al., 2014; Tjernström et al., 2012). Improving the current understanding of the Arctic boundary layer is therefore crucial for clarifying the mechanisms of Arctic climate change under continued warming and for assessing its broader impacts on the global climate system.

The vertical structure of the Arctic boundary layer is controlled by multiple factors, including mechanisms that maintain stable stratification in the Arctic, cloud-boundary-layer interactions, and the dynamical effects of low-level jets. Previous studies show that neutral and stable boundary layers dominate in the Arctic, and that the persistent surface-based temperature inversion and longwave radiative cooling are the primary mechanisms maintaining the boundary layer in a near-neutral state (Tjernström et al., 2019). Statistically, Arctic inversion-layer heights are mainly concentrated at approximately 200-300 m (Peng et al., 2023). These inversions decouple the surface from the free atmosphere and suppress the upward propagation of surface warming, thereby limiting boundary-layer development (Vihma et al., 2011; Vihma, 2014a). In summer, warm and moist air masses transport northward encounter the cold Arctic underlying surface, leading to temperature and moisture inversions and thus to shallow stable boundary layers (Rantanen et al., 2022). In winter, persistent longwave radiative cooling and the absence of solar radiation promote the widespread formation of stable boundary layers (Tjernström et al., 2019). Clouds also play an important role in modulating Arctic boundary-layer structure. Enhanced downward longwave radiation and cloud-top radiative cooling reduce atmospheric stratification stability, favoring the formation of weakly stable or near-neutral boundary layers (Peng et al., 2023). The annual mean occurrence probability of Arctic clouds is about 85%, with low clouds being dominant. Low stratiform clouds are common in summer, whereas low stratocumulus clouds occur intermittently in winter (Intrieri et al., 2002). Compared with clear-sky conditions, cloudy conditions exert a surface-warming effect during most of the year and are associated with higher boundary-layer heights (Peng et al., 2023). Another key factor affecting boundary-layer height is the low-level jet. Arctic low-level jets occur frequently and are commonly defined as wind-speed maxima with core heights below 1.5 km (Tuononen et al., 2015). Their height distribution is broad, their annual occurrence frequency exceeds 40\% (Cheng et al., 2015; Jakobson et al., 2013), and both their frequency and mean wind speed are substantially higher in the cold season than in the warm season. The strong wind shear generated by

https://doi.org/10.5194/egusphere-2026-4501
Preprint. Discussion started: 17 August 2026

low-level jets can induce intense turbulent mixing below the jet core, thereby promoting boundary-layer development (Persson et al., 2002).

Several observational techniques are currently available for diagnosing atmospheric boundary layer height, including lidar (Jordan et al., 2010), wind profiling radar (Beyrich and Leps, 2012), infrared hyperspectral radiometers (Ye et al., 2022), microwave radiometers (Cimini et al., 2022), and radiosondes (Peng et al., 2023; Jozef et al., 2023; Chan and Wood, 2013). However, under the specific environmental conditions of the Arctic, each single-instrument approach is subject to substantial limitations. Lidar and ceilometer signals are strongly attenuated by low clouds, ice fog, and liquid fog droplets, and they generally cannot penetrate optically thick clouds to retrieve boundary-layer structures above cloud top (Wiegner and Geiß, 2012; Shupe, 2011). Wind profiling radar and other ground-based wind-profile remote sensors are affected by near-surface blind zones, the lowest effective detection height, and ground clutter. Because the Arctic stable boundary layer is often extremely shallow, ranging from a few tens of metres to less than 100 m, such instruments alone are usually insufficient for fully characterizing near-surface boundary layer height (Mahrt, 2014; Tjernström et al., 2012; Illingworth et al., 2019). Infrared hyperspectral radiometers primarily rely on atmospheric thermal infrared radiance. Their sensitivity to the thermodynamic structure above clouds is substantially reduced in the presence of thick or low clouds, and large uncertainties remain in temperature and humidity profile retrievals under the strong stable stratification and near-surface inversion conditions that are common in the Arctic (Devasthale et al., 2011; Turner and Löhnert, 2014; Turner and Blumberg, 2019). Although microwave radiometers can partly penetrate non-precipitating clouds and provide temperature and humidity profile information, the information content and vertical resolution of their retrievals are limited, which makes it difficult to resolve the fine vertical structure within shallow boundary layers (Martinet et al., 2015; Illingworth et al., 2019). Radiosondes provide profiles with high vertical resolution, but their use in the Arctic is constrained by sparse observing stations, limited launch frequency, and the lack of long-term continuous observations over drifting sea ice. As a result, they cannot adequately capture rapid spatiotemporal variations in boundary layer height (Seidel et al., 2010; Vihma et al., 2014b; Brooks et al., 2017).

Single instruments have their own limitations in the complex Arctic environment (Emeis et al., 2008; Kotthaus et al., 2023), whereas multi-source active and passive remote sensing can provide complementary information on thermodynamic state, humidity, the vertical structure of clouds and aerosols, and wind fields, offering an important data basis for continuous Arctic boundary layer height retrieval (Shupe et al., 2011; Turner and Löhnert, 2014). However, because different instruments differ in temporal resolution, vertical resolution, error characteristics, and weather applicability, and because the relationships between these observations and boundary layer height are strongly nonlinear, traditional retrieval methods based on fixed thresholds or a single physical indicator cannot fully exploit the synergies of multi-source observations. Machine learning can learn complex mappings from high-dimensional data and thus offers a new technical pathway for boundary layer height retrieval. Previous studies have shown that machine learning can improve the accuracy and robustness of boundary-layer parameter estimation and boundary layer height retrieval (de Arruda Moreira et al., 2022; Guo et al., 2021). For example, Guo et al. (2021) combined machine learning with high-resolution radiosondes, ERA5, and NASA

https://doi.org/10.5194/egusphere-2026-4501
Preprint. Discussion started: 17 August 2026

Global Land Data Assimilation System products to construct a global continuous ABLH dataset over land. Xi et al. (2024) used random forests and MOSAiC radiosonde data to correct Arctic ERA5 boundary layer height, reducing the central root mean square error from 268 m to 135 m, with R^2=0.60. Nevertheless, these studies mainly focus on correcting and merging radiosonde or reanalysis data, and they do not fully exploit multimodal remote-sensing profile observations from lidar, infrared hyperspectral radiometers, and microwave radiometers during MOSAiC. They also cannot systematically characterize the coupled multivariate features under typical Arctic boundary-layer conditions such as strong inversions, cloud shielding, and shallow stratification. Therefore, this study aims to develop a deep-learning-based multi-source remote-sensing fusion framework to achieve continuous and high-accuracy retrieval of Arctic atmospheric boundary layer height using the integrated MOSAiC observations and to further reveal boundary layer–cloud interaction processes.

The remainder of this paper is organized as follows. Sect.2 briefly introduces the MOSAiC expedition and the observational data used in this study. Sect. 3 describes the machine-learning method developed for determining ABLH. Sect. 4 evaluates the model performance and presents the ablation experiments and feature-importance analysis. Sect. 5 analyzes the distribution characteristics and driving factors of the boundary layer during MOSAiC. Conclusions are given in Sect. 6.

2 Datasets

2.1 Radiosonde and Interpolated Sounding Product

This study uses atmospheric profiles obtained from Vaisala RS41 radiosondes launched during MOSAiC(Shupe et al., 2022) from September 2019 to October 2020, together with the ARM INTERPSONDE product, to construct reference labels and training samples for boundary layer height retrieval. The sondes were released from the helicopter deck of R/V Polarstern at an altitude of about 12 m and were routinely launched every 6 h at nominal times of 05:00, 11:00, 17:00, and 23:00 UTC (Maturilli et al., 2021). Figure 1 shows the location of each radiosonde launch throughout the MOSAiC year. The radiosonde observations provide high-vertical-resolution profiles of temperature, humidity, pressure, wind speed, and wind direction, which are well suited for characterizing near-surface inversions, humidity jumps, wind shear, and stable stratification that are closely related to boundary layer height.

https://doi.org/10.5194/egusphere-2026-4501
Preprint. Discussion started: 17 August 2026

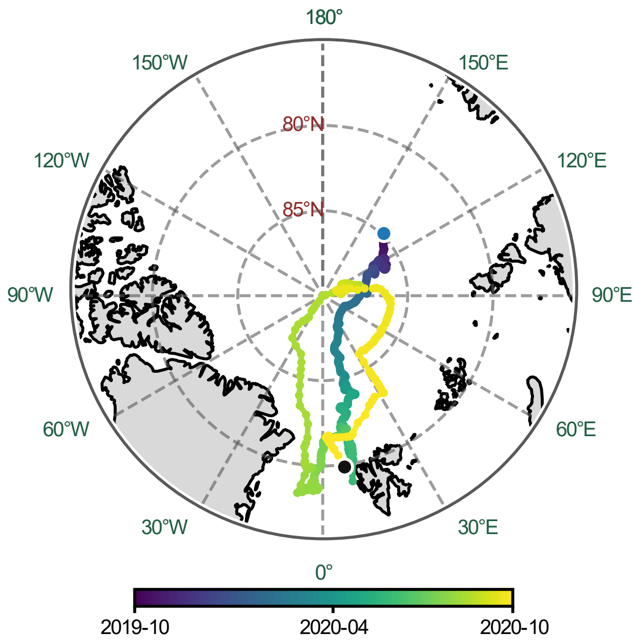

Figure 1. Map of the central Arctic, color-coded by date, with blue dots marking the starting point and black dots marking the end point.

Because the routine radiosonde sampling frequency is limited, the ARM INTERPSONDE product is additionally used to provide continuous training samples. This product interpolates MOSAiC radiosonde observations to a unified time and height grid for temperature, humidity, pressure, and wind profiles, and it constrains the temperature and humidity profiles with the MWRRET microwave radiometer retrieval product, providing atmospheric profiles at 1 min resolution (ARM, 2021). In this study, the temperature, humidity, pressure, and wind speed profiles from INTERPSONDE are used to diagnose the reference ABLH with the Richardson number method. It should be noted that this ABLH is not a directly observed absolute truth, but a reference label determined jointly from the interpolated profiles and stability criteria. To reduce the influence of sounding interpolation and temporal dependence on model evaluation, samples within 1 h before and after each radiosonde launch are treated as an independent validation set, while the remaining samples are used for model training and testing.

2.2 Microwave Radiometer

This study uses brightness temperature observations from two microwave radiometers operated during MOSAiC, namely HATPRO (Ricaud et al., 2010) and MiRAC-P (Mech et al., 2019), as passive microwave input features for the deep learning model. HATPRO includes seven channels in the K-band from 22.24 to 31.4 GHz and seven channels in the V-band from

51.26 to 58 GHz. MiRAC-P includes six G-band channels near 183.31 GHz, as well as two higher-frequency channels at 243 GHz and 340 GHz(Walbröl et al., 2022). Because Arctic boundary layer height is often affected by low clouds, fog, and humidity stratification, microwave radiometers can still provide continuous observations under cloudy conditions. They therefore help compensate for information loss in optical remote sensing under cloud obstruction and improve the model's ability to identify moist and cloudy boundary-layer states (Rosenkranz, 1998).

2.3 Atmospheric Emitted Radiance Interferometer

Atmospheric Emitted Radiance Interferometer (AERI) observations are used to provide infrared hyperspectral radiance features that constrain the vertical structure of boundary-layer temperature and water vapor. In this study, downward infrared radiance measurements from AERI are employed. To reduce the dimensionality of the hyperspectral data and minimize inter-channel redundancy, each candidate channel is first normalized and then selected using the minimum redundancy maximum relevance method (mRMR, Peng et al., 2006). This method jointly considers the relevance of each channel to the target variable and the redundancy among channels. A total of 50 AERI channels are ultimately retained as model inputs to enhance the representation of boundary-layer thermodynamic structure and inversion features. The final 50 selected channels are listed in Table 1.

Table 1. Fifty infrared channels selected by the mRMR method, ranked by importance.

Serial number	wavenymber cm^{-1}	Serial number	wavenymber cm^{-1}	Serial number	wavenymber cm^{-1}	Serial number	wavenymber cm^{-1}	Serial number	wavenymber cm^{-1}
1	547.23	**11**	1327.35	**21**	563.14	**31**	1337.95	**41**	539.52
2	1339.88	**12**	1253.10	**22**	1294.08	**32**	546.75	**42**	1304.69
3	1255.99	**13**	540.96	**23**	674.52	**33**	558.32	**43**	1262.74
4	680.79	**14**	1289.74	**24**	1257.92	**34**	1260.81	**44**	675.97
5	1291.67	**15**	617.14	**25**	1299.86	**35**	1281.54	**45**	569.89
6	550.12	**16**	1279.13	**26**	539.04	**36**	650.41	**46**	561.21
7	1250.68	**17**	1342.78	**27**	576.16	**37**	1276.24	**47**	1338.92
8	1297.4	**18**	540.48	**28**	1255.02	**38**	545.30	**48**	1254.06
9	559.29	**19**	683.68	**29**	639.80	**39**	1250.20	**49**	1268.04
10	617.63	**20**	1252.13	**30**	1255.51	**40**	1340.36	**50**	658.61

2.4 Lidar Ceilometer

Lidar ceilometer observations are used to describe cloud base height and the vertical structure of aerosols and clouds near the surface, and they serve as important auxiliary information for identifying cloud-related boundary-layer states. This study uses the backscatter data from a Vaisala CL31 lidar ceilometer (ARM User Facility, 2019) deployed on the P deck of R/V Polarstern at an altitude of about 20 m during MOSAiC, together with cloud base height data as auxiliary input.

https://doi.org/10.5194/egusphere-2026-4501
Preprint. Discussion started: 17 August 2026

3 Methodology

3.1 Data Preprocessing

This study focuses on the retrieval of atmospheric boundary layer height (ABLH) over the central Arctic Ocean during the MOSAiC drift campaign and develops a multi-branch neural network model based on multi-source observations. The model integrates active remote sensing, passive remote sensing, wind profiles, and auxiliary cloud information, and it retrieves ABLH in a condition-adaptive manner according to sky conditions. Sky conditions are classified into clear-sky, foggy, and cloudy categories using the lidar ceilometer product, in order to represent differences in boundary-layer structure and remote-sensing sensitivity under different cloud and fog conditions.

The input features of the neural network consist of multi-source observations and auxiliary parameters. The passive remote-sensing inputs include brightness temperatures from 22 channels of the HATPRO and MiRAC microwave radiometers, together with 50 channel-selected AERI infrared hyperspectral radiance channels. The active remote-sensing input is the lidar ceilometer backscatter profile, which has a vertical resolution of 10 m. The dynamical inputs are the INTERPSONDE horizontal wind profiles, including 100 vertical levels for both the u and v wind components. These wind profiles and the backscatter profiles jointly cover the altitude range from near the surface to 2 km. The auxiliary inputs include cloud base height, cloud state, and related validity flags.

During data preprocessing, a non-negative constraint is first applied to the lidar ceilometer backscatter signal, with negative values truncated to zero. A logarithmic compression transformation, $x'=\ln(1+x)$, is then applied to reduce the influence of extreme values on model training. To further reduce interference from local spikes and instrumental noise in the vertical-gradient features, percentile-based thresholding is applied to the differenced sequence between adjacent height levels. The smoothed profile is then reconstructed through cumulative summation, which improves the stability of the structural features derived from the backscatter profile (Steyn et al., 1999; Heese et al., 2010).

In addition to the original observations, several physically based features are constructed to enhance the model's ability to represent changes in boundary-layer structure. These features include wind speed, wind direction, and vector shear statistics calculated from the wind profiles, gradient, curvature, and characteristic-height information extracted from the backscatter profiles, and spectral-shape statistical features derived from the microwave and infrared radiance channels. These derived features are combined with the original observations and used as inputs to the neural network for condition-adaptive ABLH retrieval.

3.2 Determination of Reference Labels

The Richardson number (Ri) method has been shown to be one of the most suitable approaches for BLH climatological analysis because it is applicable to both stable and convective boundary layers (Guo et al., 2016; Guo et al., 2024). In the Arctic, this method also shows better consistency with manually identified ABLH reference data (Jozef et al., 2024; Peng et

https://doi.org/10.5194/egusphere-2026-4501
Preprint. Discussion started: 17 August 2026

al., 2023). Ri is a dimensionless number that characterizes the ratio between turbulence generated by thermal buoyancy and turbulence generated by mechanical wind shear, and it is commonly defined as follows (Vogelezang and Holtslag, 1996):

$$Ri_{\mathrm{F}} = \frac{(g/\theta_{\mathrm{vs}})(\theta_{\mathrm{vh}}-\theta_{\mathrm{vs}})(h-z_{\mathrm{s}})}{(u_{\mathrm{h}}-u_{\mathrm{s}})^2+(v_{\mathrm{h}}-v_{\mathrm{s}})^2+bu_*^2}, \qquad (0.1)$$

where z_s is the lower boundary of the atmospheric boundary layer (ABL),θ_{vs}, u_s, and v_s are the virtual potential temperature and horizontal wind components at height z_s, respectively, b is an empirical coefficient, and u_* is the surface friction velocity. θ_{vz} denotes the virtual potential temperature at height z, while u_z and v_z are the horizontal wind components at height z.

To determine ABLH from the Richardson number (*Ri*) profile, a critical Ri value must be specified in advance. Following Peng et al. (2023), the critical *Ri* value is set to 0.35 in this study, and zs is set to 30 m. The ABLH is then identified as the first height at which *Ri* exceeds the critical value and remains above this threshold for the next four consecutive vertical levels (Jozef et al., 2024). Figure 2 shows the boundary-layer height determined by the Richardson number method and classifies the boundary layer into stable boundary layer (SBL), neutral boundary layer (BNL), and convective boundary layer (CBL) following Liu and Liang (2012).

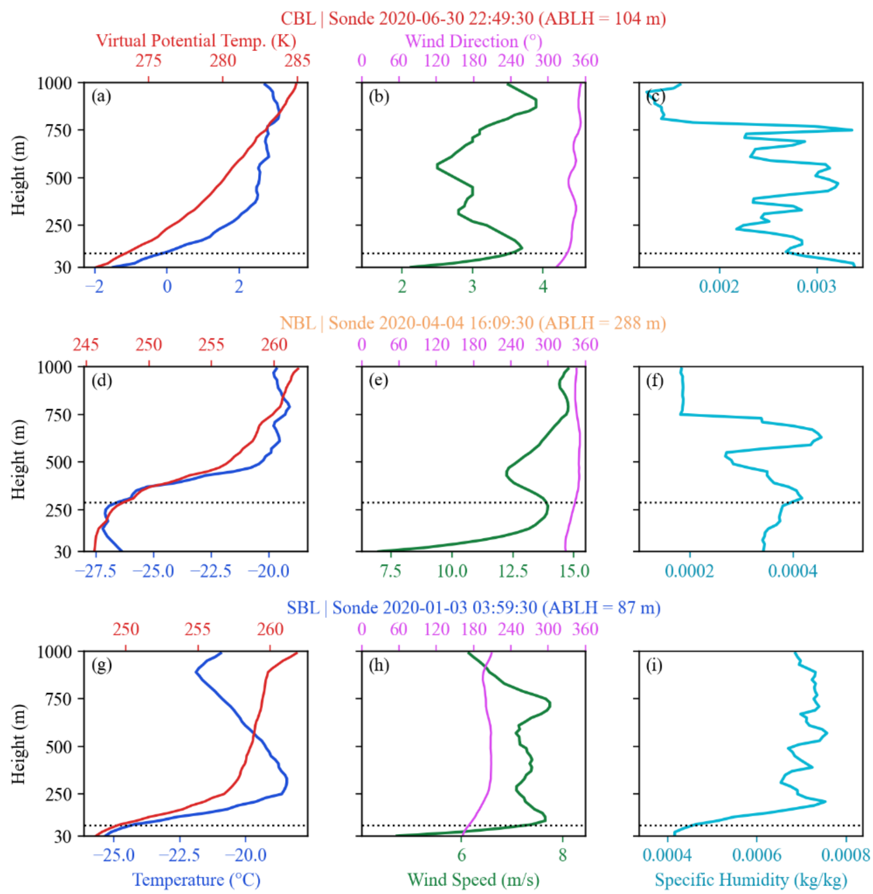

https://doi.org/10.5194/egusphere-2026-4501
Preprint. Discussion started: 17 August 2026

Figure 2. Panels (a), (d), and (g) show air temperature (blue) and potential temperature profiles (red); panels (b), (e), and (h) show wind speed (green) and wind direction (pink); and panels (c), (f), and (i) show specific humidity. Panels (a–c), (d–f), and (g–i) correspond to 22:49 UTC on 30 June 2020, 16:09 UTC on 4 April 2020, and 03:59 UTC on 3 January 2020, respectively. The boundary layers at these three times represent a convective boundary layer (CBL), a near-neutral boundary layer (NBL), and a stable boundary layer (SBL), respectively. The dashed horizontal gray lines indicate the atmospheric boundary layer height estimated only from the profile shown in each panel.

3.3 Condition-Adaptive Multi-Source Neural Network (CMNN) Model Architecture

A condition-adaptive multi-source fusion neural network is developed for ABLH retrieval. Deep learning has been widely used in Earth system science and remote-sensing retrieval because it learns complex nonlinear relations from high-dimensional multi-source observations (Reichstein et al., 2019). The model comprises multi-branch feature encoders, a conditionally modulated fusion layer, a mixture-of-experts (MoE) regression head, and a conditional residual correction head (Jordan and Jacobs, 1994). Based on the information structure and physical meaning of the observations, separate encoding branches are designed for microwave radiometers, infrared radiometers, and vertical profiles.

The microwave branch processes ordered brightness-temperature channels from HATPRO and MiRAC-P. Because microwave channels are frequency-ordered with local spectral adjacency, raw brightness temperatures and their first- and second-order differences are combined as a three-channel input, and a one-dimensional convolutional encoder extracts local spectral-shape and channel-gradient features. To capture band-dependent sensitivity to boundary-layer thermodynamic structure, HATPRO K- and V-band channels are encoded separately, while MiRAC-P channels are separately processed for the 183 GHz absorption band and window channels.

The infrared branch encodes AERI hyperspectral radiances. Infrared spectra can provide boundary-layer structural information when combined with radiosondes, lidar, and other observations (Sawyer and Li, 2013). Because selected AERI channels may lack strict local physical adjacency, convolution is not used; instead, channel gating and statistical-feature projection extract key spectral information while avoiding an unnecessary local-smoothing assumption.

The profile branch processes lidar ceilometer backscatter and INTERPSONDE wind profiles. Both are represented as multi-channel inputs containing raw values and vertical-difference information, and a one-dimensional convolutional encoder extracts vertical structural features. Backscatter profiles characterize vertical variations in aerosols, clouds, and fog particles within the boundary layer, whereas the wind branch jointly encodes u and v components, horizontal wind speed, and vertical shear.

Outputs from all branches are concatenated with auxiliary physical features, cloud-state information, and weather-condition embeddings, then fed into the conditionally modulated fusion layer. This layer uses fully connected mappings, LayerNorm, GELU activation, and residual blocks (Apicella et al., 2021), with weather conditions introduced through feature-wise linear modulation (FiLM). FiLM scales and shifts intermediate features according to external conditions, improving adaptability to different weather states (Perez et al., 2018).

https://doi.org/10.5194/egusphere-2026-4501
Preprint. Discussion started: 17 August 2026

At the output stage, an MoE regression head and conditional residual correction head are applied. The MoE conditionally weights multiple expert submodels through a gating network, enabling heterogeneous state-dependent mappings (Masoudnia and Ebrahimpour, 2014; Shazeer et al., 2017; Fedus et al., 2022). Here, expert weights are generated from weather conditions, and expert regression outputs are combined by weighted averaging.

3.4 Loss Function

To address the tendency for high boundary layers to be underestimated in ABLH retrieval and the imbalance of samples across different weather conditions, a composite loss function is used to train the model. This loss function is dominated by an asymmetric Huber loss and is combined with an MSE term and a relative-error term, so that absolute error, relative error, and residual-direction bias are constrained simultaneously. Higher weights are assigned to underestimated samples to reduce the systematic underestimation of high boundary layers. During training, sample weights are further specified according to weather type, ABLH height interval, and their combination, which increases the contribution of minority weather conditions and difficult height ranges to parameter updates. The total loss consists of a sample-level weighted loss and a batch-level distribution constraint, the latter of which is used to constrain prediction bias and dispersion under different weather conditions. The model is trained with the AdamW optimizer, and the optimal model is selected based on validation-set loss. Early stopping is triggered when the validation loss does not decrease for several consecutive epochs. The data processing workflow and the schematic of the neural network are shown in Figure 3.

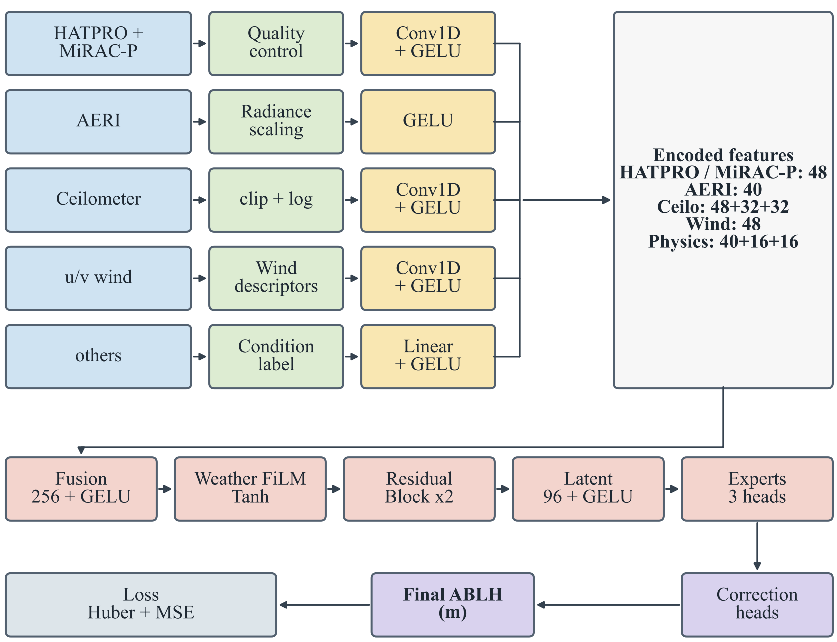

Figure 3. Schematic diagram of the CMNN model architecture and data processing.

https://doi.org/10.5194/egusphere-2026-4501
Preprint. Discussion started: 17 August 2026

4 Results

4.1 retrieval performance and importance analysis

This section evaluates the ABLH retrieval performance of the trained conditionally modulated fusion neural network (CMNN). The model inputs include microwave radiometer brightness temperatures, AERI infrared hyperspectral radiance channels, lidar ceilometer backscatter profiles, INTERPSONDE wind profiles, and auxiliary information such as cloud state. It should be noted that the training labels are diagnosed from INTERPSONDE profiles using the Richardson number method, and the input also includes INTERPSONDE wind-field information. Therefore, the test-set results mainly reflect the model's generalization capability for samples not used in training within the same continuous sample system, whereas the independent validation based on raw radiosonde profiles is used to examine its independent consistency with radiosonde observations. The test set contains 7421 samples, and the independent radiosonde validation set contains 835 radiosonde profiles. Both datasets are evaluated separately under clear-sky, cloudy, and foggy conditions. The results show that CMNN achieves good ABLH retrieval performance in both the test set and the independent validation set, with the lowest errors under clear-sky conditions. Errors increase under cloudy and foggy conditions, where a certain tendency toward underestimation is also observed. In the test set, the RMSE is 12.2 m under clear-sky conditions and increases to 26.8 m and 18.9 m under cloudy and foggy conditions, respectively. The results of the independent validation set are shown in Fig. 4. The RMSE values under clear-sky, cloudy, and foggy conditions are 15.6 m, 57.2 m, and 28.3 m, respectively, with correlation coefficients higher than 0.85 in all three categories. These results indicate that the model retrievals are highly consistent with radiosonde-diagnosed ABLH. The performance differences may arise because clouds and fog weaken the effective sensitivity of AERI to temperature and humidity profiles and alter the backscatter structure observed by the lidar ceilometer, thereby increasing uncertainty in ABLH identification.

https://doi.org/10.5194/egusphere-2026-4501
Preprint. Discussion started: 17 August 2026

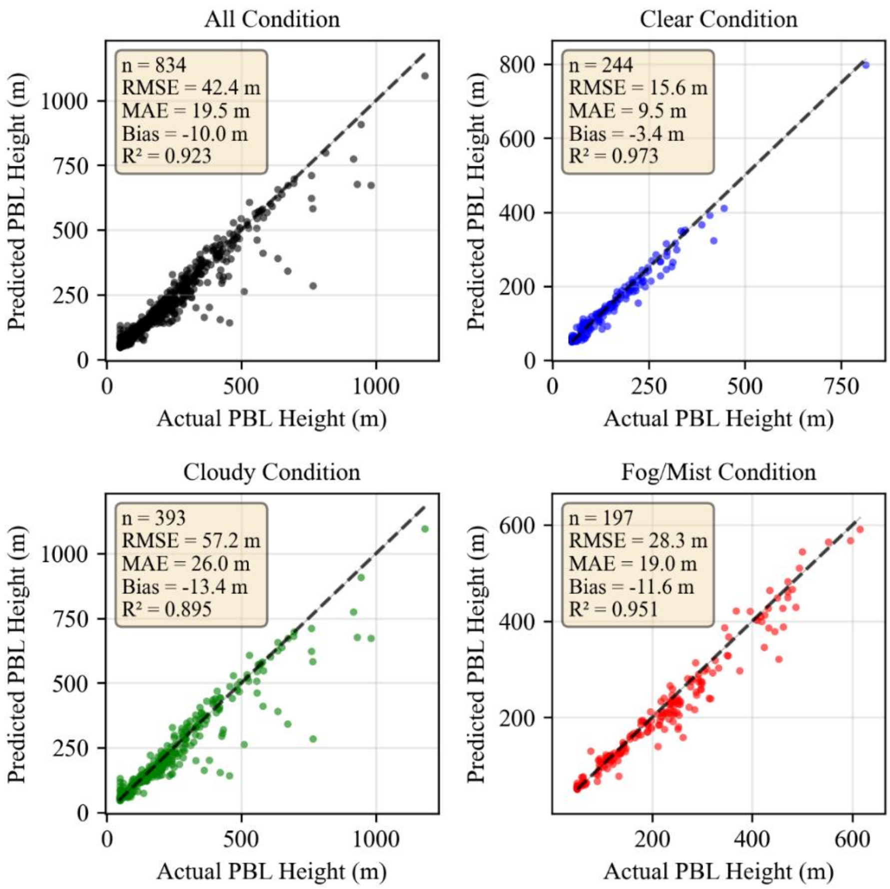

Figure 4. Correlation between the CMNN-retrieved height and the Ri method height in the independent radiosonde dataset, shown for overall (black), clear-sky (blue), cloudy (green), and foggy (red) conditions.

To quantitatively assess the contributions of different input information to ABLH retrieval, this study uses the SHapley Additive exPlanations (SHAP, Lundberg et al., 2017) method to analyze the importance of original and derived features, and further applies single-source removal ablation experiments to examine the influence of each observation type on model performance. The SHAP results shown in Figure 5 indicate that wind-field-related features contribute the most to the retrieval results, accounting for about 48.2% of the total contribution. This is related to the sensitivity of the Richardson number method to wind-speed shear. The ablation experiments shown in Fig. 6 also show that removing wind-field information causes the most pronounced model degradation. In particular, under foggy and cloudy conditions, the RMSE increases by 30.0 m and 21.9 m, respectively, indicating that the mechanical mixing and vertical-shear information provided by wind profiles are key constraints for identifying the boundary layer top under stable boundary-layer and low-visibility conditions.

https://doi.org/10.5194/egusphere-2026-4501
Preprint. Discussion started: 17 August 2026

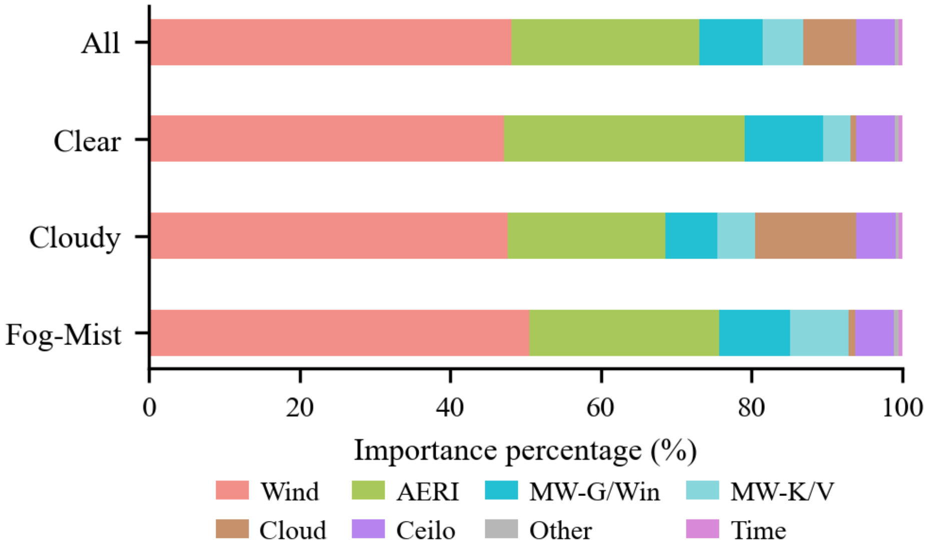

Figure 5. SHAP importance ranking under different conditions in the independent radiosonde validation dataset.

Figure 6. Ablation experiment results. The numbers in the figure represent the change in each evaluation metric (horizontal axis) for the given weather condition and experimental setting (vertical axis) relative to the corresponding metric of the full model.

https://doi.org/10.5194/egusphere-2026-4501
Preprint. Discussion started: 17 August 2026

Infrared hyperspectral observations are the second most important information source, and their role shows clear weather dependence. Under clear-sky conditions, the SHAP contribution of AERI increases to 32.1%. After AERI is removed, the RMSE increases by 4.4 m, indicating that infrared radiance strongly represents near-surface inversions, thermal stratification, and surface cooling processes, which is beneficial for ABLH identification under clear-sky or weak-cloud conditions. By contrast, under cloudy conditions, adding AERI instead increases the RMSE, suggesting that cloud shielding and re-emission effects in infrared radiative transfer may introduce additional uncertainty. The relatively high SHAP importance of AERI under cloudy conditions indicates that infrared information is frequently used by the model, but its contribution direction and effectiveness are affected by cloud structure. It provides constraints through cloud-base thermal-radiance features, sub-cloud low-level temperature and humidity states, and thermal stratification information.

Microwave radiometers mainly provide supplementary constraints for ABLH retrieval through temperature and humidity profile information. Their overall SHAP contribution is about 13.8%, and removing microwave observations only slightly increases the RMSE under different weather conditions, suggesting that their role is relatively stable but not dominant. Among the microwave channels, the MiRAC-P 183 GHz absorption-band channels contribute more strongly, indicating that information related to water vapor and cloud liquid water from high-frequency channels is relatively sensitive to boundary-layer-top identification.

The lidar ceilometer provides direct information on the vertical scattering structure, but its overall SHAP contribution is relatively low, at about 5.2%. This may be because the reference ABLH in this study is not directly determined from the aerosol backscatter gradient. Nevertheless, the ceilometer still plays a stabilizing role under cloudy and foggy conditions. After removing the ceilometer, the RMSE increases by 3.61 m and 3.29 m under cloudy and foggy conditions, respectively, indicating that it provides important structural constraints for cloud–boundary-layer coupling, complex scattering structures, and cases where the cloud base is close to the boundary layer top. In particular, under cloudy conditions, it helps distinguish the relative position between the boundary layer top and cloud layers.

Overall, the SHAP analysis and ablation experiments show that CMNN does not rely equally on all types of observations, but dynamically adjusts the weights of different information sources according to weather conditions. Wind-field information provides the primary dynamical constraint, infrared observations contribute strongly under clear-sky conditions, microwave observations provide stable thermodynamic and humidity-related supplementary information, and the ceilometer and cloud-state information enhance vertical-structure identification under cloudy and foggy conditions. The complementary effects of multi-source observations improve the applicability and stability of the model under complex Arctic boundary-layer conditions.

To further illustrate how these condition-dependent sensitivities are reflected in actual retrievals, a representative early-May case was examined, as shown in Fig. 7. During P1 (1–5 May), low-level equivalent potential temperature was relatively low, wind speed was weak, relative humidity was high, and near-surface temperature was low. The retrieved ABLH remained low overall, indicating a cold and stable boundary layer with suppressed turbulent mixing. In P2 (5–11 May), ABLH variability increased markedly and repeatedly rose to moderate and high values. Meanwhile, wind speed increased and thermodynamic

https://doi.org/10.5194/egusphere-2026-4501
Preprint. Discussion started: 17 August 2026

conditions improved, suggesting that buoyancy and mechanical turbulence jointly promoted boundary-layer development. However, when cloud-base height changed rapidly or approached the boundary-layer top, the retrieved ABLH showed short-term jumps, reflecting interference from cloud-related moist layers and stratified structures. In P3 (11–15 May), near-surface temperature continued to rise and the pressure field adjusted noticeably, while ABLH further increased overall, indicating gradual development into a deeper and more mature mixed layer.

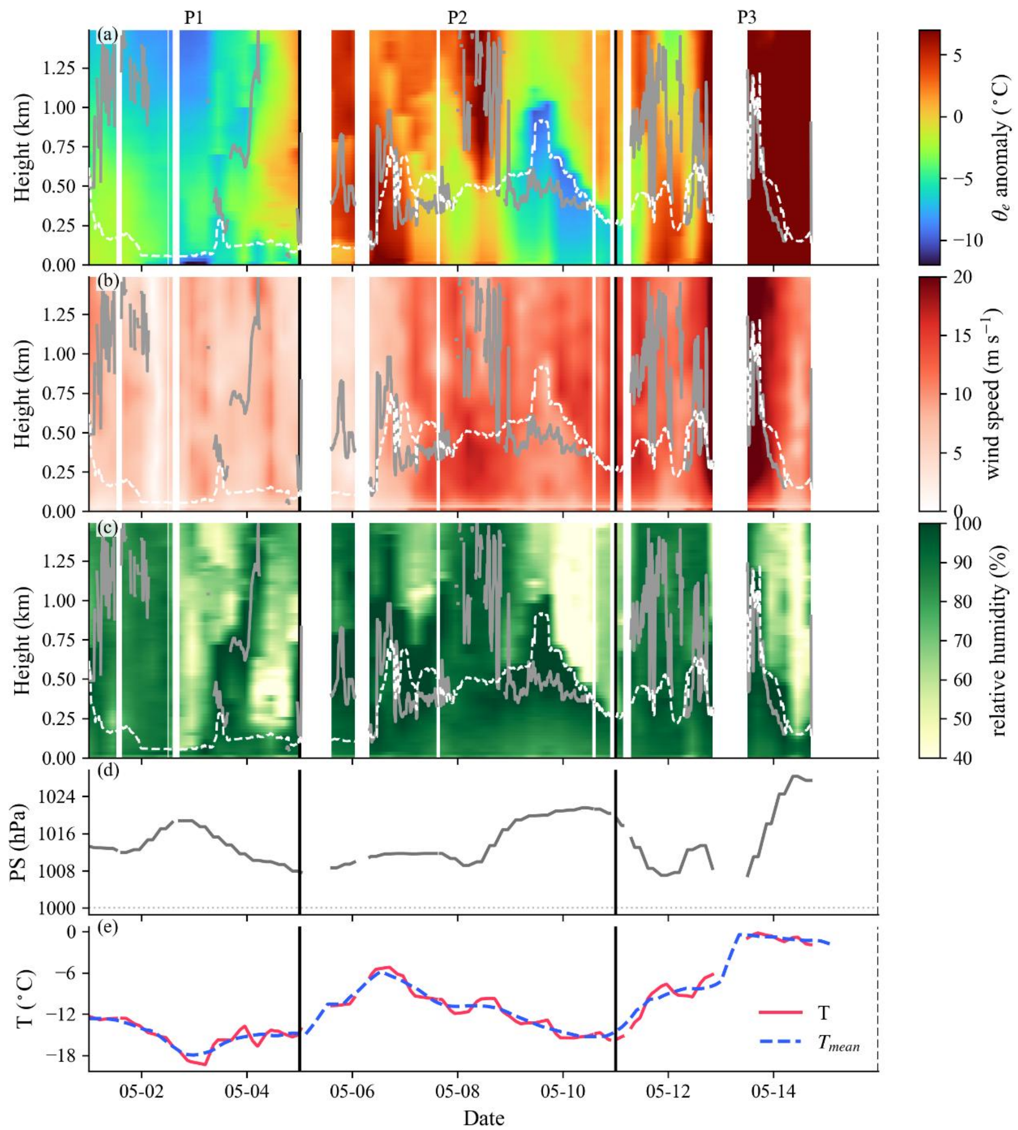

Figure 7. Case study during 1–15 May 2020 in the MOSAiC period. In panels (a), (b), and (c), the gray lines indicate cloud base height, and the white solid lines indicate boundary-layer height determined by the CMNN method. The background fields in panels (a), (b), and (c) are potential temperature, wind speed, and relative humidity, respectively. Panel (d) shows surface pressure, and panel (e) shows surface temperature (red line) and 2 m air temperature (blue line).

https://doi.org/10.5194/egusphere-2026-4501
Preprint. Discussion started: 17 August 2026

4.2 Temporal variability of ABLH from daily to seasonal scales

During MOSAiC, ABLH exhibited pronounced seasonal variability, reaching its maximum in May with a median value of 321 m, then decreasing rapidly in June and showing low values in July and January, as shown in Fig. 8. This variability is closely related to the seasonal evolution of the near-surface thermodynamic structure in the Arctic. In winter, the absence of solar radiation leads to continuous surface cooling and the formation of strong inversions, which suppress turbulent development and generally result in a shallow ABLH. The potential temperature profiles also reflect this stable stratification: in January, the potential temperature gradient within the 0–1 km layer reaches 16.8 K*km^{-1}, corresponding to a monthly mean ABLH of only about 140 m. In spring, increasing solar radiation weakens near-surface stability, enhances convective and turbulent mixing, and substantially reduces the near-surface gradient to about 4.0 K*km^{-1} in May. Accordingly, ABLH reaches its peak in May. Although summer is characterized by polar-day conditions, sea-ice melt and the heat-capacity effect of the ocean limit near-surface warming and turbulent development, causing ABLH to decrease again. In autumn, increased cloud occurrence and synoptic disturbances reorganize the boundary-layer structure, leading to higher ABLH than in summer. Overall, stronger near-surface stability generally corresponds to a shallower boundary layer, whereas weaker stability favors boundary-layer deepening.

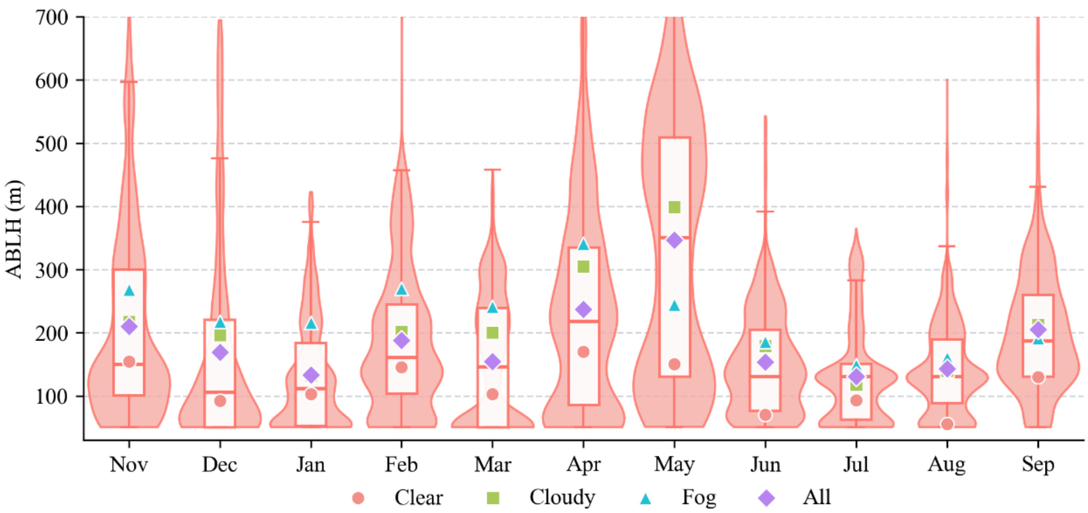

Figure 8. Monthly distribution of the ABLH derived from MOSAiC. Pink violins show the overall distribution density; embedded white boxplots indicate the 25th, 50th, and 75th percentiles. Colored symbols denote monthly mean ABLH under different weather conditions.

Figure 8 also shows the monthly mean boundary layer height under different weather conditions. The mean ABLH under cloudy and foggy conditions is generally higher than that under clear-sky conditions, indicating that clouds and fog may promote boundary-layer development through processes such as longwave radiative warming, reduced near-surface stability, and enhanced turbulent mixing. The difference is most pronounced in May, when the mean ABLH values under clear-sky and cloudy conditions are 142.81 m and 362.51 m, respectively, with a difference of about 219.70 m. High cloud occurrence

https://doi.org/10.5194/egusphere-2026-4501
Preprint. Discussion started: 17 August 2026

in September and March corresponds to relatively high ABLH in these months, further suggesting that clouds play an important regulatory role in Arctic boundary-layer structure.

In terms of diurnal variation, the response of ABLH to near-surface temperature shows clear seasonal dependence, as shown in Fig. 9. In spring and summer, higher near-surface temperature generally corresponds to higher ABLH, indicating that surface heating enhances buoyancy-driven turbulent mixing and promotes boundary-layer development. This response is clearest in spring, and ABLH variations show a certain lag relative to temperature variations. In autumn, the diurnal pattern becomes less regular, suggesting that the boundary layer gradually shifts from being thermally dominated to being jointly controlled by thermodynamic, dynamical, and radiative processes. In winter, by contrast, the synchronous relationship between ABLH and near-surface temperature is weak, implying that wind-shear mixing, cloud longwave radiative effects, and synoptic disturbances may be more important than near-surface temperature in the polar winter stable boundary layer.

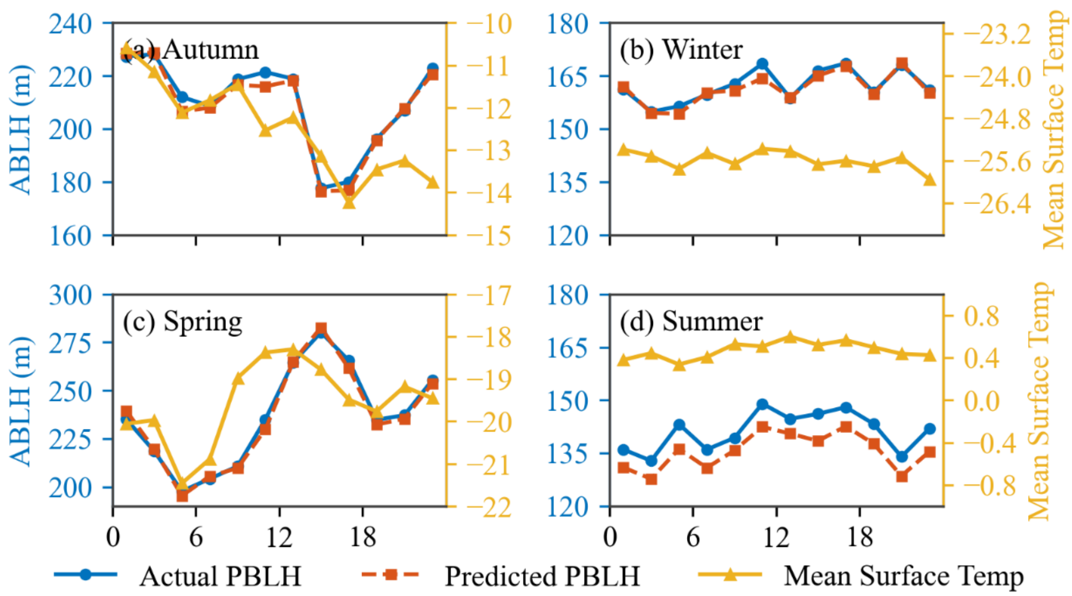

Figure 9. Diurnal variation statistics of the 2-hour mean boundary layer height in different seasons. Panels (a)–(d) show autumn, winter, spring, and summer, respectively. The blue line denotes observed ABLH, the orange dashed line denotes predicted ABLH, and the yellow line denotes mean surface temperature.

4.3 Estimation of key drivers of ABLH

According to the relative position between cloud base height (CBH) and atmospheric boundary layer height (ABLH), the weather samples are classified into three categories: clear sky, cloud, and fog. Cloudy samples are further divided into three subtypes: coupled, CBH-above-ABLH, and ABLH-above-CBH cases. Meanwhile, following the classification method of

https://doi.org/10.5194/egusphere-2026-4501
Preprint. Discussion started: 17 August 2026

Liu and Liang (2010), the boundary layer is categorized into stable, neutral, and convective boundary layers. The proportions of different boundary-layer types under different weather conditions are shown in Figure 10. The results show that the relative position between CBH and ABLH has an important influence on boundary-layer development, and this relationship exhibits clear seasonal dependence. Under coupled and CBH-above-ABLH conditions, the boundary layer is generally shallow, with seasonal mean ABLH values of about 100–300 m. For coupled low clouds, although clouds can weaken near-surface cooling by enhancing downward longwave radiation, stable stratification and low-level inversions still restrict the upward development of the boundary layer. When CBH is higher than ABLH, the cloud layer is relatively decoupled from surface-driven turbulent mixing, and its influence is mainly expressed through modulation of the radiative and thermal environment above the boundary layer. Therefore, its direct promotion of ABLH growth is limited.

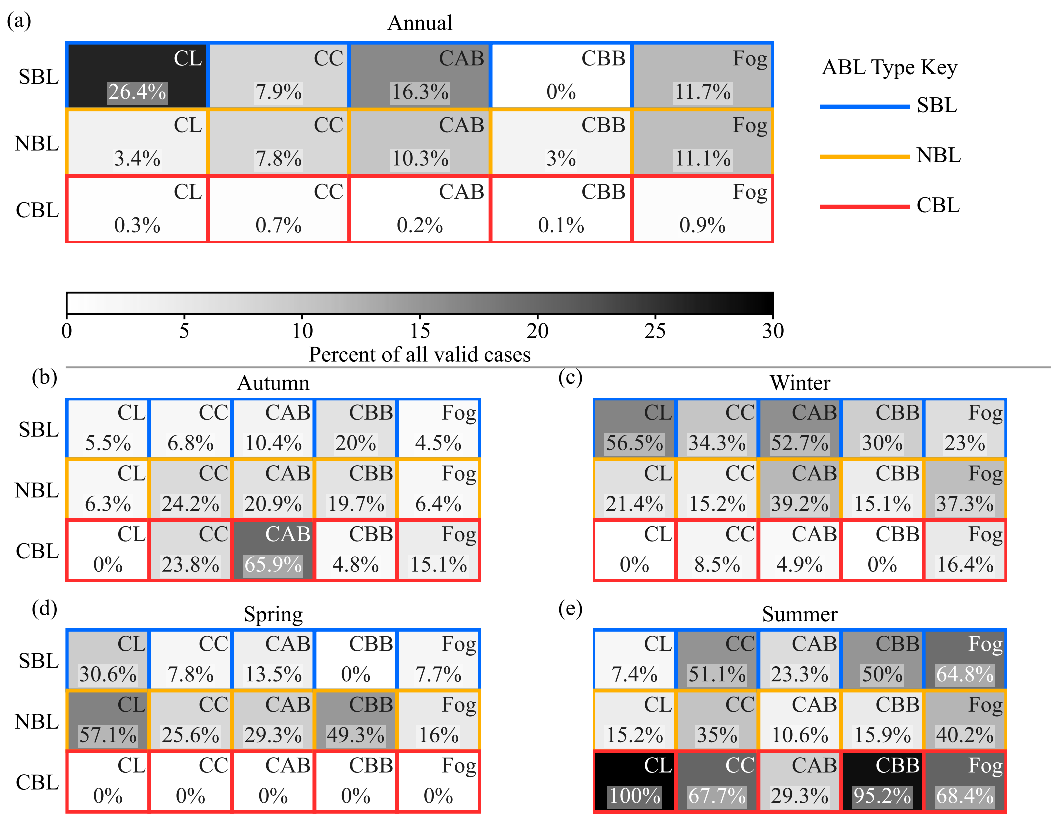

Figure 10. (a) denotes the proportion of each boundary layer type relative to the total samples. SBL: stable boundary layer; NBL: neutral boundary layer; CBL: convective boundary layer. CL: clear-sky conditions; CC: coupled cloud–boundary layer; CAB: cloud base height more than 100 m above the boundary layer height; CBB: cloud base height below the boundary layer height; fog: foggy conditions. The numbers for (b,c,d,e) represent the proportion of each boundary layer type and weather type occurring in that season relative to the annual total of that type.

https://doi.org/10.5194/egusphere-2026-4501
Preprint. Discussion started: 17 August 2026

During MOSAiC, the meteorological tower installed on the sea ice provided near-surface turbulence and meteorological observations. This study selects several dynamical, radiative, and thermodynamic variables to analyze their relationships with ABLH, as shown in Fig. 11. Overall, Arctic boundary-layer height is primarily controlled by near-surface mechanical mixing, while radiative and thermodynamic processes play a secondary modulatory role.

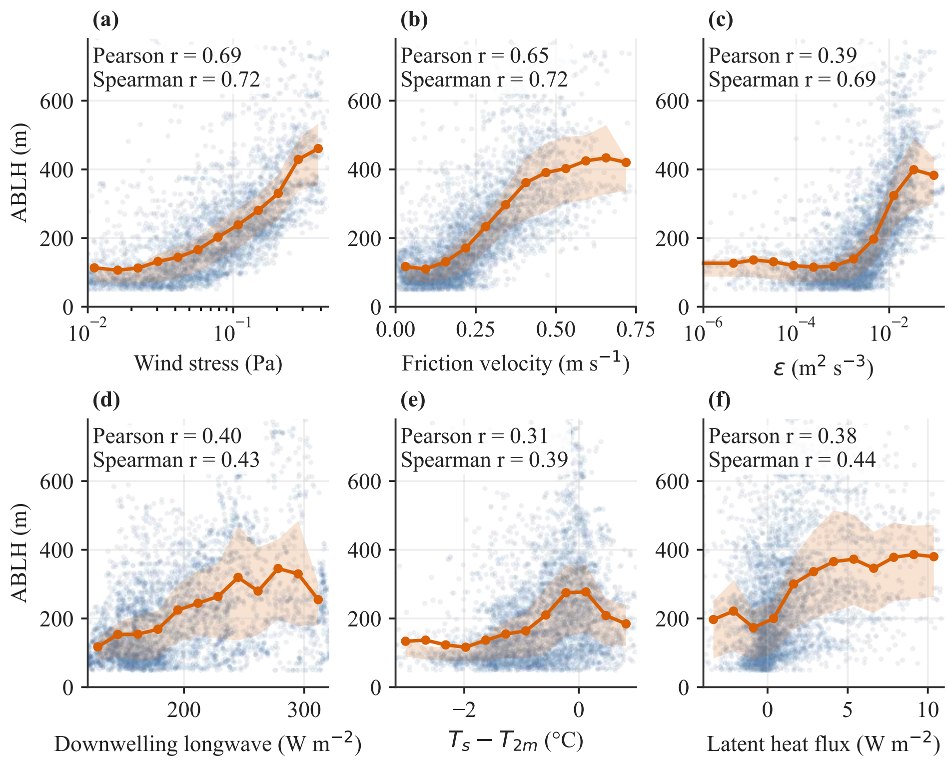

Figure 11. Correlation analysis between boundary layer height and surface meteorological station measurements. (a) wind shear stress, (b) friction velocity, (c) turbulence dissipation rate, (d) downward longwave radiation, (e) difference between surface temperature and 2 m temperature, (f) latent heat flux.

Wind stress and friction velocity show the strongest correlations with ABLH, with Pearson correlation coefficients of 0.69 and 0.65, respectively. This indicates that when near-surface momentum transport and shear-driven turbulence intensify, vertical mixing is enhanced and the boundary-layer top rises accordingly. This mechanism is particularly important in the Arctic, where stable stratification dominates and buoyancy-driven turbulence is suppressed, so boundary-layer development depends more strongly on mechanical mixing. Turbulent kinetic energy dissipation rate further supports this conclusion. Its Pearson correlation with ABLH is 0.39, while the Spearman rank correlation reaches 0.69, suggesting a pronounced nonlinear relationship. In other words, ABLH does not increase linearly with turbulence intensity, but responds more clearly only after turbulence becomes strong enough to erode the stable layer.

https://doi.org/10.5194/egusphere-2026-4501
Preprint. Discussion started: 17 August 2026

By contrast, radiative and thermodynamic variables are more weakly correlated with ABLH, but they remain physically meaningful. Downward longwave radiation is positively correlated with ABLH (r = 0.40), indicating that increased cloud cover or higher atmospheric humidity may weaken surface radiative cooling and thus reduce near-surface inversions. The surface-air temperature difference, Ts - T2m, is also positively correlated with ABLH (r = 0.31), suggesting that a relatively warmer surface favors boundary-layer development. Latent heat flux shows a moderate correlation with ABLH (r = 0.38), which may reflect the promoting effect of enhanced surface-atmosphere coupling under moist or cloudy conditions on boundary-layer deepening. Overall, mechanical mixing is the dominant factor controlling ABLH variability during MOSAiC, while radiative and thermodynamic processes mainly influence boundary-layer height by regulating near-surface stability.

An LLJ was defined following Stull (1988) as a local maximum in wind speed that exceeds the wind speeds at levels above it by more than 2 m /s. As shown in Figure 12, low-level jets (LLJs) substantially deepen the Arctic boundary layer. During MOSAiC, LLJs occurred with a frequency of 47.3%. The mean ABLH was 249.6 m under LLJ conditions and 181.6 m in the absence of LLJs, corresponding to a mean increase of 68.0 m. This deepening occurs under all examined weather conditions, with increases of approximately 35 m under clear-sky conditions, 68 m under cloudy conditions, and 83 m under fog or haze conditions. The ABLH is strongly and positively correlated with LLJ core wind speed (r = 0.73), whereas its correlation with LLJ core height is negligible. This indicates that LLJs promote boundary-layer growth mainly by enhancing low-level wind shear and mechanical turbulent mixing, rather than by directly determining the boundary-layer top through the height of the jet core. On the monthly scale, LLJ frequency covaries with the mean ABLH, further supporting the role of LLJs as an important dynamical factor in Arctic boundary-layer deepening.

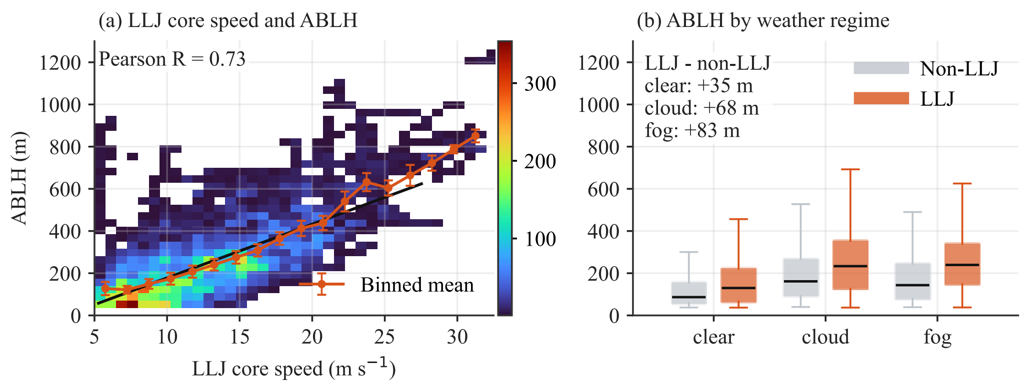

Figure 12. (a) Scatter plot between low-level jet (LLJ) core speed and ABLH, (b) boxplots of boundary layer height under the three weather conditions with and without LLJs, with the vertical axes of both panels sharing the same meaning and scale.

4.4 Model Extrapolation Results

The NSA (North Slope of Alaska) site is located on the Alaska North Slope and serves as an important long-term observing station in the terrestrial Arctic, providing an observational environment independent of MOSAiC. Because NSA and MOSAiC differ in underlying surface, climate background, and boundary-layer structure, the no-microwave-band model is

https://doi.org/10.5194/egusphere-2026-4501
Preprint. Discussion started: 17 August 2026

applied to the NSA dataset to evaluate its generalization capability beyond the MOSAiC training domain. It should also be noted that the reference ABLH is diagnosed from the INTERPSONDE radiosonde interpolation product using the Richardson number method, while the model inputs also include radiosonde-interpolated wind profiles. Although this may introduce some non-independence, wind profiles represent shear and mechanical mixing, which are key physical controls on boundary-layer height; therefore, their use is physically justified.

On the MOSAiC radiosonde validation set, the no-microwave model reproduces ABLH variations well. As shown in Figure 13, the model performs well overall (n = 834, RMSE = 46.6 m, R^2 = 0.907). Retrieval skill is highest under clear-sky and fog/haze conditions, with RMSE values of 20.6 m and 34.6 m and R^2 values of 0.954 and 0.926, respectively, while errors are larger under cloudy conditions (RMSE = 61.3 m, R^2 = 0.880). When the same no-microwave configuration is transferred to the NSA dataset, model performance decreases but remains effective for ABLH retrieval (n = 35,567, RMSE = 76.2 m, R^2 = 0.771). Results remain relatively stable under clear-sky and fog/haze conditions, with RMSE values of 41.7 m and 50.2 m and R^2 values of 0.855 and 0.866, respectively, whereas the largest degradation occurs under cloudy conditions (RMSE = 100.7 m, R^2 = 0.693). These results indicate that, despite substantial environmental differences between MOSAiC and NSA, the model retains meaningful cross-site generalization capability. They also support the feasibility of using radiosonde-interpolated wind profiles in both reference-label construction and model training: rather than causing the model to rely only on MOSAiC-specific label relationships, these profiles provide physically meaningful shear and mechanical-mixing information that remains transferable at an independent Arctic site. Overall, the NSA test validates the cross-site applicability of the no-microwave configuration, while microwave observations can provide additional thermodynamic constraints to further improve retrieval accuracy and robustness.

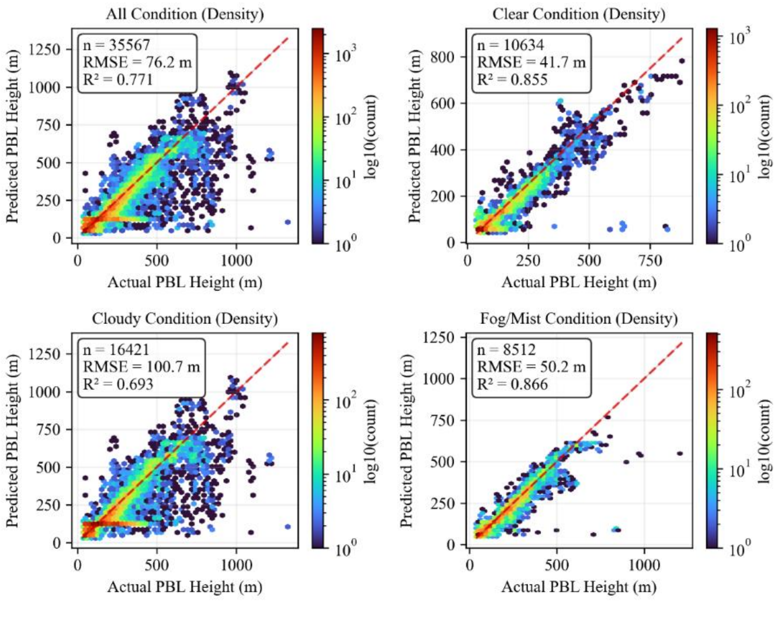

Figure 13. Applicability of the CMNN at the NSA site.

https://doi.org/10.5194/egusphere-2026-4501
Preprint. Discussion started: 17 August 2026

5 Conclusion and Discussion

In this study, we used year-round MOSAiC observations to develop a condition-adaptive, multi-source neural network framework for retrieving the atmospheric boundary layer height (ABLH) over the central Arctic Ocean. The framework integrates microwave radiometer, infrared hyperspectral radiometer, ceilometer, wind profiler, and auxiliary cloud information, with training labels generated by an improved Richardson number method under different cloud conditions. The results show that this active-passive fusion framework can capture the main variations in Arctic ABLH and provide physically meaningful information on dynamical, thermodynamical, and cloud-related processes.

The model shows strong retrieval skill, with an overall RMSE of 42.4 m and an R2 of 0.923 under the microwave-enhanced MOSAiC configuration. Performance is best under clear-sky conditions and weakest under cloudy conditions, where cloud-affected structures introduce the largest uncertainty. SHAP analysis indicates that wind-related variables dominate the retrieval, contributing approximately 48.2% of the total importance. Infrared observations are most important under clear skies, microwave observations provide stable constraints under moist and cloud-affected conditions, and ceilometer information becomes useful when cloud-base height is close to the boundary-layer top.

Daily and monthly statistics show that cloud effects on Arctic ABLH are strongly state dependent. Coupled and CBH-above-ABLH cases generally correspond to shallow boundary layers, with seasonal mean ABLH values of about 100-300 m, whereas ABLH-above-CBH cases are associated with much deeper boundary layers, reaching 617 m in winter and 592 m in spring. These results indicate that cloud impacts depend on the relative position of the cloud layer and boundary-layer top, rather than acting as a simple suppressing or enhancing factor.

The driving-factor analysis shows that Arctic ABLH variability during MOSAiC is controlled mainly by mechanical mixing, with radiative and thermodynamic processes playing secondary roles. Wind stress and friction velocity show the strongest positive correlations with ABLH, while turbulent kinetic energy dissipation indicates a nonlinear response of boundary-layer growth to turbulence intensity. Downward longwave radiation, surface-air temperature difference, and latent heat flux further modulate ABLH by regulating near-surface stability and surface-atmosphere coupling. LLJs also promote boundary-layer deepening: their occurrence increases the mean ABLH from 181.6 m to 249.6 m, mainly by enhancing low-level wind shear and mechanically generated turbulence.

The NSA extrapolation experiment confirms that the no-microwave configuration retains meaningful transferability beyond the MOSAiC domain. Although performance decreases from an RMSE of 46.6 m and an R2 of 0.907 on the MOSAiC radiosonde validation set to an RMSE of 76.2 m and an R2 of 0.771 at NSA, the model remains effective, especially under clear-sky and fog or haze conditions. This cross-site test suggests that the framework captures transferable physical controls on ABLH, while microwave observations can further improve robustness by adding thermodynamic constraints.

Code and data availability

Availability StatementAll data used in this work is publicly available. The retrieval results and related code presented in this paper can be downloaded from https://doi.org/10.5281/zenodo.21449016. The Lidar Ceilometer, radiosonde, INTERPSONDE product, and infrared hyperspectral data were obtained from the ARM Data Discovery platform (https://adc.arm.gov/discovery/). These can be found by searching keywords or selecting the corresponding MOSAiC site. The HATPRO data were downloaded from the study by Walbröl et al. (2022), which is publicly shared via PANGAEA at https://doi.org/10.1594/PANGAEA.941356. The MiRAC-P data were also downloaded from Walbröl et al. (2022) and are publicly shared via PANGAEA at https://doi.org/10.1594/PANGAEA.941407. The near-surface atmospheric data from the meteorological tower and the radiation station data are available at the National Science Foundation's Arctic Data Center (Cox et al., 2023a) at https://doi.org/10.18739/A2PV6B83F. The validation data for the NSA site were obtained from the ARM Data Discovery platform (https://adc.arm.gov/discovery/).

Author contributions

Yuliang Liu: Conceptualization, Methodology, Software, Validation, Formal analysis, Investigation, Data Curation, Writing – Original Draft, Visualization.

Shulei Li: Supervision, Project administration, Funding acquisition, Writing – Review & Editing.

Lei Liu: Resources, Supervision.

Shuai Hu: Resources, Supervision.

Xuyang Li: Data Curation, Validation.

Rongying Shao: Validation, Investigation.

All authors reviewed the manuscript and approved the final version..

Competing interests

The authors declare that they have no competing interests.

Disclaimer

Copernicus Publications adds a standard disclaimer: “Copernicus Publications remains neutral with regard to jurisdictional claims made in the text, published maps, institutional affiliations, or any other geographical representation in this paper.

https://doi.org/10.5194/egusphere-2026-4501
Preprint. Discussion started: 17 August 2026

While Copernicus Publications makes every effort to include appropriate place names, the final responsibility lies with the authors. Views expressed in the text are those of the authors and do not necessarily reflect the views of the publisher."
Please feel free to add disclaimer text at your choice, if applicable.

Financial support

This work was supported by National Natural Science Foundation of China under Grants No. 42575155 and No. 42430604.

References

Akansu, E. F., Dahlke, S., Siebert, H., and Wendisch, M.: Evaluation of methods to determine the surface mixing layer height of the atmospheric boundary layer in the central Arctic during polar night and transition to polar day in cloudless and cloudy conditions, ATMOSPHERIC CHEMISTRY AND PHYSICS, 23, 15473–15489, https://doi.org/10.5194/acp-23-15473-2023, 2023.

Apicella, A., Donnarumma, F., Isgrò, F., and Prevete, R.: A survey on modern trainable activation functions, Neural Netw., 138, 14-32, https://doi.org/10.1016/j.neunet.2021.01.026, 2021.

Atmospheric Radiation Measurement (ARM) User Facility: Ceilometer (CEIL), ARM Mobile Facility (MOS) MOSAIC, compiled by Morris, V., Zhang, D., and Ermold, B., ARM Data Center [data set], https://doi.org/10.5439/1181954, 2019.

Atmospheric Radiation Measurement (ARM) User Facility: Interpolated Sonde (INTERPOLATEDSONDE), ARM Mobile Facility (MOS) MOSAIC, compiled by Jensen, M., Giangrande, S., Fairless, T., and Zhou, A., ARM Data Center [data set], https://doi.org/10.5439/1095316, 2021.

Beyrich, F. and Leps, J.-P.: An operational mixing height data set from routine radiosoundings at Lindenberg: Methodology, Meteorol. Z., 21, 337–348, https://doi.org/10.1127/0941-2948/2012/0333, 2012.

Brooks, I. M., Tjernström, M., Persson, P. O. G., Shupe, M. D., Atkinson, R. A., Canut, G., Birch, C. E., Mauritsen, T., Sedlar, J., and Brooks, B. J.: The Turbulent Structure of the Arctic Summer Boundary Layer During The Arctic Summer Cloud-Ocean Study, Journal of Geophysical Research: Atmospheres, 122, 9685-9704, https://doi.org/10.1002/2017JD027234, 2017.

Chan, K. M. and Wood, R.: The seasonal cycle of planetary boundary layer depth determined using COSMIC radio occultation data, J. Geophys. Res.-Atmos., 118, 12422–12434, https://doi.org/10.1002/2013JD020147, 2013.

Cheng, G., Gao, Z. Q., Zheng, Y. F., et al. : A study on low level jets and temperature inversion over the Arctic Ocean by using SHEBA data, Climatic and Environmental Research, 2013.

https://doi.org/10.5194/egusphere-2026-4501
Preprint. Discussion started: 17 August 2026

Cimini, D., De Angelis, F., Dupont, J.-C., Pal, S., and Haeffelin, M.: Mixing layer height retrievals by multichannel microwave radiometer observations, Atmospheric Measurement Techniques, 6, 2941–2951, https://doi.org/10.5194/amt-6-2941-2013, 2013.

Cox, C. J., Gallagher, M., Shupe, M., Persson, O., Blomquist, B., Grachev, A., Riihimaki, L., Kutchenreiter, M., Morris, V., Solomon, A., Brooks, I., Costa, D., Gottas, D., Hutchings, J., Osborn, J., Morris, S., Preusser, A., and Uttal, T.: Met City meteorological and surface flux measurements (Level 3 Final), Multidisciplinary Drifting Observatory for the Study of Arctic Climate (MOSAiC), central Arctic, October 2019–September 2020, Arctic Data Center [data set], https://doi.org/10.18739/A2PV6B83F, 2023a.

de Arruda Moreira, G., Sánchez-Hernández, G., Guerrero-Rascado, J. L., Cazorla, A., and Alados-Arboledas, L.: Estimating the urban atmospheric boundary layer height from remote sensing applying machine learning techniques, Atmos. Res., 266, 105962, https://doi.org/10.1016/j.atmosres.2021.105962, 2022.

Devasthale, A., Sedlar, J., and Tjernström, M.: Characteristics of water-vapour inversions observed over the Arctic by Atmospheric Infrared Sounder (AIRS) and radiosondes, ATMOSPHERIC CHEMISTRY AND PHYSICS, 11, 9813–9823, https://doi.org/10.5194/acp-11-9813-2011, 2011.

Emeis, S., Schäfer, K., and Münkel, C.: Surface-based remote sensing of the mixing-layer height – a review, Meteorol. Z., 17, 621–630, https://doi.org/10.1175/BAMS-88-10-1608, 2008.

Fedus, W., Zoph, B., and Shazeer, N.: Switch Transformers: Scaling to trillion parameter models with simple and efficient sparsity, Journal of Machine Learning Research, 23, https://doi.org/10.48550/arXiv.2101.03961 1–39, 2022.

Graversen, R. G., Mauritsen, T., Tjernström, M., Källén, E., and Svensson, G.: Vertical structure of recent Arctic warming, Nature, 451, 53–56, https://doi.org/10.1038/nature06502, 2008.

Guo, J., Miao, Y., Zhang, Y., Liu, H., Li, Z., Zhang, W., He, J., Lou, M., Yan, Y., and Bian, L.: The climatology of planetary boundary layer height in China derived from radiosonde and reanalysis data, ATMOSPHERIC CHEMISTRY AND PHYSICS, 16, 13309–13319, https://doi.org/10.5194/acp-16-13309-2016, 2016.

Guo, J., Zhang, J., Yang, K., Liao, H., Zhang, S., Huang, K., Lv, Y., Shao, J., Yu, T., and Tong, B.: Investigation of near-global daytime boundary layer height using high-resolution radiosondes: first results and comparison with ERA5, MERRA-2, JRA-55, and NCEP-2 reanalyses, ATMOSPHERIC CHEMISTRY AND PHYSICS, 21, 17079–17097, https://doi.org/10.5194/acp-21-17079-2021, 2021.

Guo, J., Zhang, J., Shao, J., Chen, T., Bai, K., Sun, Y., Li, N., Wu, J., Li, R., and Li, J.: A merged continental planetary boundary layer height dataset based on high-resolution radiosonde measurements, ERA5 reanalysis, and GLDAS, Earth System Science Data, 16, 1–14, https://doi.org/10.5194/essd-16-1-2024, 2024.

Han, S., Bian, H., Tie, X., Xie, Y., Sun, M., and Liu, A. : Impact of nocturnal planetary boundary layer on urban air pollutants: measurements from a 250 m tower over Tianjin, China, Journal of Hazardous Materials, 162, 264–269, https://doi.org/10.1016/j.jhazmat.2008.05.056, 2009.

Heese, B., Flentje, H., Althausen, D., Ansmann, A., and Frey, S.: Ceilometer lidar comparison: backscatter coefficient retrieval and signal-to-noise ratio determination, Atmos. Meas. Tech., 3, 1763-1773, https://doi.org/10.5194/amt-3-1763-2010, 2010.

Heinemann, G., Schefczyk, L., Zentek, R., Brooks, I. M., Dahlke, S., and Walbröl, A.: Evaluation of Vertical Profiles and Atmospheric Boundary Layer Structure Using the Regional Climate Model CCLM during MOSAiC, Meteorology 2, 257–275, https://doi.org/10.3390/meteorology2020016, 2023.

Illingworth, A. J., Cimini, D., Haefele, A., Haeffelin, M., Hervo, M., Kotthaus, S., Löhnert, U., Martinet, P., Mattis, I., O'Connor, E. J., and Potthast, R. : How can existing ground based profiling instruments improve European weather forecasts?, Bulletin of the American Meteorological Society, 100, 605–619, https://doi.org/10.1175/BAMS-D-17-0231.1, 2019.

Intrieri, J. M., Shupe, M. D., Uttal, T., and McCarty, B. J.: An annual cycle of Arctic cloud characteristics observed by radar and lidar at SHEBA, J. Geophys. Res.-Oceans, 107, SHE 5-1–SHE 5-15, https://doi.org/10.1029/2000JC000423, 2002.

Jacobs, R. A., Jordan, M. I., Nowlan, S. J., and Hinton, G. E.: Adaptive mixtures of local experts, Neural Comput., 3, 79-87, https://doi.org/10.1162/neco.1991.3.1.79, 1991.

Jakobson, L., Vihma, T., Jakobson, E., Palo, T., Männik, A., and Jaagus, J.: Low-level jet characteristics over the Arctic Ocean in spring and summer, ATMOSPHERIC CHEMISTRY AND PHYSICS, 13, 11089–11099, https://doi.org/10.5194/acp-13-11089-2013, 2013.

Jordan, M. I. and Jacobs, R. A.: Hierarchical mixtures of experts and the EM algorithm, Neural Comput., 6, 181-214, https://doi.org/10.1162/neco.1994.6.2.181, 1994.

Jordan, N. S., Hoff, R. M., and Bacmeister, J. T.: Validation of Goddard Earth Observing System-version 5 MERRA planetary boundary layer heights using CALIPSO, J. Geophys. Res., 115, D24108, https://doi.org/10.1029/2009JD013777, 2010.

Jozef, G., Cassano, J., Dahlke, S., and de Boer, G.: Testing the efficacy of atmospheric boundary layer height detection algorithms using uncrewed aircraft system data from MOSAiC, Atmospheric Measurement Techniques, 15, 4001–4022, https://doi.org/10.5194/amt-15-4001-2022, 2022.

Jozef, G. C., Cassano, J. J., Dahlke, S., Dice, M., Cox, C. J., and de Boer, G.: Thermodynamic and kinematic drivers of atmospheric boundary layer stability in the central Arctic during the Multidisciplinary drifting Observatory for the Study of Arctic Climate (MOSAiC), ATMOSPHERIC CHEMISTRY AND PHYSICS, 23, 13087–13106, https://doi.org/10.5194/acp-23-13087-2023, 2023.

Jozef, G. C., Cassano, J. J., Dahlke, S., Dice, M., Cox, C. J., and de Boer, G. : An overview of the vertical structure of the atmospheric boundary layer in the central Arctic during MOSAiC, Atmospheric Chemistry and Physics, 24, 1429–1450, https://doi.org/10.5194/acp-24-1429-2024, 2024.

Kotthaus, S., Bravo-Aranda, J. A., Collaud Coen, M., Guerrero-Rascado, J. L., Costa, M. J., Cimini, D., O'Connor, E. J., Hervo, M., Alados-Arboledas, L., Jiménez-Portaz, M., Mona, L., Ruffieux, D., Illingworth, A. J., and Haeffelin, M.:

https://doi.org/10.5194/egusphere-2026-4501
Preprint. Discussion started: 17 August 2026

Atmospheric boundary layer height from ground-based remote sensing: a review of capabilities and limitations, Atmos. Meas. Tech., 16, 433–479, https://doi.org/10.5194/amt-16-433-2023, 2023.

Lauvaux, T., Miles, N. L., Deng, A., Richardson, S. J., Cambaliza, M. O., Davis, K. J., Gaudet, B., Gurney, K. R., Huang, J., and O'Keefe, D.: High-resolution atmospheric inversion of urban CO2 emissions during the dormant season of the Indianapolis Flux Experiment (INFLUX), Journal of Geophysical Research: Atmospheres, 121, 5213–5236, https://doi.org/10.1002/2015JD024473, 2016.

Liu, S. and Liang, X.-Z.: Observed diurnal cycle climatology of planetary boundary layer height over the contiguous United States, Journal of Climate, 23, 5790–5809, https://doi.org/10.1175/2010JCLI3552.1, 2010.

Lundberg, S. M. and Lee, S.-I.: A unified approach to interpreting model predictions, in: Advances in Neural Information Processing Systems 30, edited by: Guyon, I., Luxburg, U. V., Bengio, S., Wallach, H., Fergus, R., Vishwanathan, S., and Garnett, R., Curran Associates, Inc., Red Hook, NY, 2017, pp. 4765-4774.

Mahrt, L.: Stably stratified atmospheric boundary layers, ANNUAL REVIEW OF FLUID MECHANICS, 46, 23–45, https://doi.org/10.1146/annurev-fluid-010313-141354, 2014.

Marsik, F. J., Fischer, K. W., McDonald, T. D., and Samson, P. J. : Comparison of methods for estimating mixing height used during the 1992 Atlanta field intensive, Journal of Applied Meteorology, 34, 1802–1814, https://doi.org/10.1175/1520-0450(1995)034<1802:COMFEM>2.0.CO;2 , 1995.

Martinet, P., Cimini, D., De Angelis, F., Canut, G., Unger, V., Guillot, R., Tzanos, D., and Paci, A.: Combining ground-based microwave radiometer and the AROME convective scale model through 1DVAR retrievals in complex terrain: an Alpine valley case study, ATMOSPHERIC MEASUREMENT TECHNIQUES, 8, 3385–3402, https://doi.org/10.5194/amt-8-3385-2015, 2015.

Masoudnia, S. and Ebrahimpour, R.: Mixture of experts: a literature survey, Artif. Intell. Rev., 42, 275-293, https://doi.org/10.1007/s10462-012-9338-y, 2014.

Matveeva, T. A. and Semenov, V. A.: Regional Features of the Arctic Sea Ice Area Changes in 2000–2019 versus 1979–1999 Periods, Atmosphere, 13, 1434, https://doi.org/10.3390/atmos13091434, 2022.

Maturilli, M., Holdridge, D. J., Dahlke, S., Graeser, J., Sommerfeld, A., Jaiser, R., Deckelmann, H., and Schulz, A. : Initial radiosonde data from 2019-10 to 2020-09 during project MOSAiC, PANGAEA, https://doi.org/10.1594/PANGAEA.928656, 2021.

Mech, M., Kliesch, L.-L., Anhäuser, A., Rose, T., Kollias, P., and Crewell, S.: Microwave Radar/radiometer for Arctic Clouds (MiRAC): first insights from the ACLOUD campaign, Atmospheric Measurement Techniques, 12, 5019–5037, https://doi.org/10.5194/amt-12-5019-2019, 2019.

Peng, H., Long, F., and Ding, C.: Feature selection based on mutual information: criteria of max-dependency, max-relevance, and min-redundancy, IEEE Trans. Pattern Anal. Mach. Intell., 27, 1226–1238, https://doi.org/10.1109/TPAMI.2005.159, 2005.

Peng, S., Yang, Q., Shupe, M. D., Xi, X., Han, B., Chen, D., Dahlke, S., and Liu, C.: The characteristics of atmospheric boundary layer height over the Arctic Ocean during MOSAiC, Atmospheric Chemistry and Physics, 23, 8683–8703, https://doi.org/10.5194/acp-23-8683-2023, 2023.

Perez, E., Strub, F., de Vries, H., Dumoulin, V., and Courville, A.: FiLM: Visual reasoning with a general conditioning layer, Proceedings of the AAAI Conference on Artificial Intelligence, 32, 3942–3951, 2018.

Persson, P. O. G., Fairall, C. W., Andreas, E. L., Guest, P. S., and Perovich, D. K.: Measurements near the Atmospheric Surface Flux Group tower at SHEBA: Near-surface conditions and surface energy budget, Journal of Geophysical Research: Oceans, 107, 8045, https://doi.org/10.1029/2000JC000705, 2002.

Rantanen, M., Karpechko, A. Y., Lipponen, A., Nordling, K., Hyvärinen, O., Ruosteenoja, K., Vihma, T., and Laarksonen, A.: The Arctic has warmed nearly four times faster than the globe since 1979, Commun. Earth & Env., 3, 168, https://doi.org/10.1038/s43247-022-00498-3, 2022.

Reichstein, M., Camps-Valls, G., Stevens, B., Jung, M., Denzler, J., Carvalhais, N., and Prabhat: Deep learning and process understanding for data-driven Earth system science, Nature, 566, 195–204, https://doi.org/10.1038/s41586-019-0912-1, 2019.

Ricaud, P., Gabard, B., Derrien, S., Chaboureau, J.-P., Rose, T., Mombauer, A., and Czekala, H.: HAMSTRAD-Tropo, A 183-GHz Radiometer Dedicated to Sound Tropospheric Water Vapor Over Concordia Station, Antarctica, IEEE Transactions on Geoscience and Remote Sensing, 48, 1365–1380, https://doi.org/10.1109/TGRS.2009.2029345, 2010.

Rosenkranz, P. W. : Water vapor microwave continuum absorption: a comparison of measurements and models, Radio Science, 33, 919–928, https://doi.org/10.1029/98RS01167, 1998.

Sawyer, V. and Li, Z.: Detection, variations and intercomparison of the planetary boundary layer depth from radiosonde, lidar and infrared spectrometer, ATMOSPHERIC ENVIRONMENT, 79, 518–528, https://doi.org/10.1016/j.atmosenv.2013.07.019, 2013.

Seidel, D. J., Ao, C. O., and Li, K.: Estimating climatological planetary boundary layer heights from radiosonde observations: comparison of methods and uncertainty analysis, JOURNAL OF GEOPHYSICAL RESEARCH: ATMOSPHERES, 115, D16113, https://doi.org/10.1029/2009JD013680, 2010.

Shazeer, N., Mirhoseini, A., Maziarz, K., Davis, A., Le, Q., Hinton, G., and Dean, J.: Outrageously large neural networks: The sparsely-gated mixture-of-experts layer, International Conference on Learning Representations, 2017.

Shupe, M. D.: Clouds at Arctic atmospheric observatories. Part II: Thermodynamic phase characteristics, JOURNAL OF APPLIED METEOROLOGY AND CLIMATOLOGY, 50, 645–661, https://doi.org/10.1175/2010JAMC2468.1, 2011.

Shupe, M. D., Rex, M., Blomquist, B., Persson, P. O. G., Schmale, J., Uttal, T., et al.. Overview of the MOSAiC expedition: Atmosphere. Elementa: Science of the Anthropocene, 10(1), 00060. https://doi.org/10.1525/elementa.2021.00060, 2022.

Steyn, D. G., Baldi, M., and Hoff, R. M.: The detection of mixed layer depth and entrainment zone thickness from lidar backscatter profiles, J. Atmos. Oceanic Technol., 16, 953-959, https://doi.org/10.1175/1520-0426(1999)016<0953:TDOMLD>2.0.CO;2,1999.

Stirnberg, R., Cermak, J., Kotthaus, S., Haeffelin, M., Andersen, H., Fuchs, J., Kim, M., Petit, J.-E., and Favez, O. : Meteorology driven variability of air pollution (PM_1) revealed with explainable machine learning, Atmospheric Chemistry and Physics, 21, 3919–3948, https://doi.org/10.5194/acp-21-3919-2021, 2021.

Stull, R. B. : An Introduction to Boundary Layer Meteorology, Kluwer Academic Publishers, Dordrecht, 666 pp., https://doi.org/10.1007/978-94-009-3027-8, 1988.

Sujatha, P., Mahalakshmi, D. V., Ramiz, A., Rao, P. V. N., and Naidu, C. V. : Ventilation coefficient and boundary layer height impact on urban air quality, Cogent Environmental Science, 2, 1125284, https://doi.org/10.1080/23311843.2015.1125284, 2016.

Tjernström, M., Birch, C. E., Brooks, I. M., Shupe, M. D., Persson, P. O. G., Sedlar, J., Mauritsen, T., Leck, C., Paatero, J., Szczodrak, M., and Wheeler, C. R.: Meteorological conditions in the central Arctic summer during the Arctic Summer Cloud Ocean Study (ASCOS), ATMOSPHERIC CHEMISTRY AND PHYSICS, 12, 6863–6889, https://doi.org/10.5194/acp-12-6863-2012, 2012.

Tjernström, M., Shupe, M. D., Brooks, I. M., Achtert, P., Pytherch, J., and Sedlar, J.: Arctic Summer Airmass Transformation, Surface Inversions, and the Surface Energy Budget, J. Climate, 32, 769–789, https://doi.org/10.1175/JCLI-D-18-0216.1, 2019.

Tuononen, M., Sincalair, V. A., and Vihma, T.: A climatology of low-level jets in the mid-latitudes and polar regions of the Northern Hemisphere, Q. J. Roy. Atmos. Sci. Lett., 16, 492–499, https://doi.org/10.1002/asl.587, 2015.

Turner, D. D. and Löhnert, U.: Information content and uncertainties in thermodynamic profiles and liquid cloud properties retrieved from the ground-based Atmospheric Emitted Radiance Interferometer (AERI), JOURNAL OF APPLIED METEOROLOGY AND CLIMATOLOGY, 53, 752–771, https://doi.org/10.1175/JAMC-D-13-0126.1, 2014.

Turner, D. D. and Blumberg, W. G.: Improvements to the AERIoe thermodynamic profile retrieval algorithm, IEEE JOURNAL OF SELECTED TOPICS IN APPLIED EARTH OBSERVATIONS AND REMOTE SENSING, 12, 1339–1354, https://doi.org/10.1109/JSTARS.2018.2874968, 2019.

Vajda, A., Tuomenvirta, H., Jokinen, P., Luomaranta, A., Makkonen, L., Tikanmäki, M., Groenemeijer, P., Saarikivi, P., Michaelides, S., Papadakis, M., Tymvios, F., and Athanasatos, S. : Probabilities of Adverse Weather Affecting Transport in Europe: Climatology and Scenarios up to the 2050s, Finnish Meteorological Institute, ISBN 978-951-697-762-4, 2011.

Vihma, T., Kilpeläinen, T., Manninen, M., Sjöblom, A., Jakobson, E., Palo, T., Jaagus, J., and Maturilli, M. : Characteristics of temperature and humidity inversions and low level jets over Svalbard fjords in spring, Advances in Meteorology, 2011, 486807, https://doi.org/10.1155/2011/486807, 2011.

Vihma, T. : Effects of Arctic sea ice decline on weather and climate: a review, Surveys in Geophysics, 35, 1175–1214, https://doi.org/10.1007/s10712-014-9284-0, 2014a.

Vihma, T., Pirazzini, R., Fer, I., Renfrew, I. A., Sedlar, J., Tjernström, M., Lüpkes, C., Nygård, T., Notz, D., Weiss, J., Marsan, D., Cheng, B., Birnbaum, G., Gerland, S., Chechin, D., and Gascard, J.-C.: Advances in understanding and

https://doi.org/10.5194/egusphere-2026-4501
Preprint. Discussion started: 17 August 2026

parameterization of small-scale physical processes in the marine Arctic climate system: a review, ATMOSPHERIC CHEMISTRY AND PHYSICS, 14, 9403–9450, https://doi.org/10.5194/acp-14-9403-2014, 2014b.

Vogelezang, D. H. P. and Holtslag, A. A. M. : Evaluation and model impacts of alternative boundary layer height formulations, Boundary-Layer Meteorology, 81, 245–269, https://doi.org/10.1007/BF02430331, 1996.

Walbröl, A., Crewell, S., Engelmann, R., Orlandi, E., Griesche, H., Radenz, M., Hofer, J., Althausen, D., Maturilli, M., and Ebell, K.: Atmospheric temperature, water vapour and liquid water path from two microwave radiometers during MOSAiC, Scientific Data, 9, https://doi.org/10.1038/s41597-022-01504-1, 2022.

Wesslén, C., Tjernström, M., Bromwich, D. H., de Boer, G., Ekman, A. M. L., Bai, L.-S., and Wang, S.-H. : The Arctic summer atmosphere: an evaluation of reanalyses using ASCOS data, Atmospheric Chemistry and Physics, 14, 2605–2624, https://doi.org/10.5194/acp-14-2605-2014, 2014.

Wiegner, M. and Geiß, A.: Aerosol profiling with the Jenoptik ceilometer CHM15kx, ATMOSPHERIC MEASUREMENT TECHNIQUES, 5, 1953–1964, https://doi.org/10.5194/amt-5-1953-2012, 2012.

Xi, X., Yang, Q., Liu, C., Shupe, M. D., Han, B., Peng, S., Zhou, S., and Chen, D.: Evaluation of the Planetary Boundary Layer Height From ERA5 Reanalysis With MOSAiC Observations Over the Arctic Ocean, Journal of Geophysical Research: Atmospheres, 129, https://doi.org/10.1029/2024JD040779, 2024.

Ye, J., Liu, L., Wang, Q., Hu, S., and Li, S.: A Novel Machine Learning Algorithm for Planetary Boundary Layer Height Estimation Using AERI Measurement Data, IEEE Geoscience and Remote Sensing Letters, 19, 1–5, https://doi.org/10.1109/LGRS.2021.3073048, 2022.